Estimating black carbon aging time-scales with a particle-resolved aerosol model

Nicole Riemer[a],*, Matthew West[b], Rahul Zaveri[c], Richard Easter[c]

[a]*Department of Atmospheric Sciences, University of Illinois at Urbana-Champaign, Urbana, Illinois, USA*
[b]*Department of Mechanical Science and Engineering, University of Illinois at Urbana-Champaign, Urbana, Illinois, USA*
[c]*Atmospheric Science and Global Change Division, Pacific Northwest National Laboratory, Richland, Washington, USA*

ABSTRACT

Understanding the aging process of aerosol particles is important for assessing their chemical reactivity, cloud condensation nuclei activity, radiative properties and health impacts. In this study we investigate the aging of black carbon containing particles in an idealized urban plume using a new approach, the particle-resolved aerosol model PartMC-MOSAIC. We present a method to estimate aging time-scales using an aging criterion based on cloud condensation nuclei activation. The results show a separation into a daytime regime where condensation dominates and a nighttime regime where coagulation dominates. There is also a strong dependence on supersaturation threshold. For the chosen urban plume scenario and supersaturations ranging from 0.1% to 1%, the aging time-scales vary between 11 and 0.068 h during the day, and between 54 and 6.4 h during the night.

© 2009 Elsevier Ltd. All rights reserved.

1. Introduction

Black carbon containing particles, or "soot" particles, are ubiquitous in the atmosphere and their role for regional and global climate has been widely recognized (IPCC, 2007). Since black carbon absorbs light (Horvath & Trier, 1993), it contributes to the aerosol radiative forcing, potentially partially offsetting the cooling effect of scattering aerosol particles such as sulfates (Menon, Hansen, Nazarenko, & Luo, 2002).

Black carbon containing particles originate from the incomplete combustion of carbon containing material, hence emissions from traffic are an important contributor (Bond et al., 2004). Other important sources for black carbon include biomass burning and the combustion of coal by industrial processes. In this paper we focus on black carbon from traffic emissions. Measurements of vehicle emissions from gasoline and diesel cars show that the emitted particles are a complex mixture of many chemical species with the main constituents being black carbon and organic carbon (Medalia & Rivin, 1982; Toner, Sodeman, & Prather, 2006). Trace concentrations of ionic and metallic species are also present (Kleeman, Schauer, & Cass, 2000). The exact composition depends on several factors, including the fuel type, the operating conditions and the condition of the individual vehicles.

During their transport in the atmosphere, the composition of these particle emissions are further modified. Coagulation, condensation and photochemistry are contributing processes, collectively known as aging (Weingartner, Burtscher, & Baltensperger, 1997). During this aging process the composition of the individual particles or, in other words, their mixing states change (Furutani, Dallosto, Roberts, & Prather, 2008). This impacts the particles' physico-chemical properties including their chemical reactivity, radiative properties and health impacts. In particular, the aging process can change the particles' hygroscopicity from

---

* Corresponding author.

E-mail address: nriemer@illinois.edu (N. Riemer).

initially hydrophobic to more hydrophilic, and hence change their ability to become cloud condensation nuclei (Cubison et al., 2008; McFiggans et al., 2006; McMurry & Stolzenburg, 1989; Moffet, Qin, Rebotier, Furutani, & Prather, 2008).

This is important as models and observations suggest that wet deposition represents 70–85% of the tropospheric sink for carbonaceous aerosol mass (Pöschl, 2005). As a consequence, to assess the budget and impact of black carbon, models need to capture the aging process adequately. Many global models have simulated both (fresh) hydrophobic black carbon and (aged) hydrophilic black carbon, which can be considered a minimal representation of the black carbon mixing state (Cooke, Liousse, Cachier, & Feichter, 1999; Croft, Lohmann, & von Salzen, 2005; Koch, 2001; Lohmann, Feichter, Chuang, & Penner, 1999). In such a framework only the hydrophilic black carbon is subject to in-cloud scavenging. The conversion from hydrophobic to hydrophilic is frequently modeled as a first-order system with the single parameter of aging rate or its inverse, the aging time-scale τ which represents the time-scale on which a population of black carbon containing particles transfers from the "fresh" category to the "aged" category.

While conceptually simple, the actual value of the aging time-scale τ is not well constrained. Koch (2001) and Croft et al. (2005) compared different aging parameterizations in global models and concluded that the model results critically depended on the respective formulation. Riemer, Vogel, and Vogel (2004) used mesoscale simulations to determine τ. They derived the aging time-scale for black carbon particles as a function of height and time of the day and concluded that assuming a single parameter for the black carbon aging time-scale is an oversimplification that will incorrectly estimate the black carbon burden. However, even though this treatment allowed more detailed insight into the aging process, it was still based on ad hoc aging rules inherent to the modal model framework that was used (Riemer, Vogel, Vogel, & Fiedler, 2003).

Recently, Riemer, West, Zaveri, and Easter (2009) developed a particle-resolved aerosol model, PartMC-MOSAIC, which explicitly resolves the composition of individual particles in a given population of different types of aerosol particles, so that no ad hoc aging criterion needs to be invoked. They applied PartMC-MOSAIC in a Lagrangian box-model framework to an idealized urban plume scenario to study the evolution of urban aerosols due to coagulation and condensation/evaporation over the course of 24 h.

In this study, we build upon Riemer et al. (2009) and present a method for estimating aging time-scales of black carbon containing particles using PartMC-MOSAIC, based on the idealized urban plume scenario. We take the particle population simulated in Riemer et al. (2009) and use a cloud condensation nuclei (CCN)-based aging criterion to determine whether each individual particle that contains black carbon is fresh or aged at every timestep, and how many particles transfer between the fresh and aged categories during each timestep.

We use these results to determine first-order aging time-scales as they are needed for first-order bulk models of aerosol aging. To our knowledge it is the first time that a method is presented for explicitly calculating aging time-scales without making any a priori assumptions about the aging process.

It should be pointed out that the aging criterion used here (time until a certain critical supersaturation is reached) is different from that of Riemer et al. (2004) (time until 5% of mass is hydrophilic). Both have good practical uses. The approach used here is directly applicable to the time before black carbon may be susceptible to nucleation-scavenging wet deposition in clouds, and larger accumulation-mode black carbon particles may require less than 5% hydrophilic mass in order to meet this criterion. The previous approach is useful for knowing how long it will take for black carbon particles to be classified as internally mixed, and for deriving the optical properties as done in Riemer et al. (2003).

Section 2 introduces the model system. In Section 3 we describe the idealized plume scenario that served as a basis for the time-scale estimation. Section 4 presents our method for deriving time-scales from our model and Section 5 shows the results. We summarize our findings in Section 6.

2. Model description

PartMC-MOSAIC is a particle-resolved model that simulates the evolution of individual aerosol particles and trace gases in a single parcel (or volume) of air moving along a specified trajectory. For each particle the mass of each constituent species is tracked, but the particle position in space is not simulated, making this a zero-dimensional or box model. In addition to coagulation and aerosol- and gas-phase chemistry, the model includes prescribed emissions of aerosols and gases, and mixing of the parcel with background air. The simulation results shown here use around 100 000 particles in a volume of around 16 cm^3 (the precise values vary over the course of the simulation). We regard this volume as being representative of a much larger air parcel. The model accurately predicts both number and mass size distributions and is therefore suited for applications where either quantity is required. Details of PartMC-MOSAIC and the urban plume scenario are described in Riemer et al. (2009). Here we give a brief summary.

An aerosol particle contains mass $\mu_a \geq 0$ (kg) of species a, for $a = 1, \ldots, A$, so that the particle composition is described by the A-dimensional vector $\vec{\mu} \in \mathbb{R}^A$. In our case A is 20. The cumulative aerosol number distribution at time t and constituent masses $\vec{\mu} \in \mathbb{R}^A$ is $N(\vec{\mu}, t)$ (m^{-3}), which is defined to be the number concentration of aerosol particles that contain less than μ_a mass of species a, for all $a = 1, \ldots, A$. The aerosol number distribution at time t and constituent masses $\vec{\mu} \in \mathbb{R}^A$ is $n(\vec{\mu}, t)$ (m^{-3} kg^{-A}), which is defined by

$$n(\vec{\mu}, t) = \frac{\partial^A N(\vec{\mu}, t)}{\partial \mu_1 \partial \mu_2 \ldots \partial \mu_A}. \tag{1}$$

We consider a Lagrangian parcel with volume V (m^3), also called the computational volume. We represent the aerosol state by storing N_p particles in this volume, written $\Pi = (\vec{\mu}^1, \vec{\mu}^2, \ldots, \vec{\mu}^{N_p})$, where the particle order is not significant. Each particle is an A-dimensional vector $\vec{\mu}^i \in \mathbb{R}^A$ with components $(\mu_1^i, \mu_2^i, \ldots, \mu_A^i)$, so μ_a^i is the mass of species a in particle i, for $a = 1, \ldots, A$ and $i = 1, \ldots, N_p$.

The simulation of the aerosol state proceeds by two mechanisms. First, the composition of each particle can change, changing the components of the vector $\vec{\mu}^i$ for particle i as species condense from the gas phase and evaporate to it, for example. Second, the population Π can have particles added and removed, either by emissions, dilution or coagulation events between particles. While condensation/evaporation is handled deterministically, emission, dilution and coagulation are treated with a stochastic Monte Carlo approach.

Applying such a Monte Carlo approach for simulating the evolution of particle distributions dates back to Gillespie (1975), who developed the exact Stochastic Simulation Algorithm (see also Gillespie, 1976, 1977, 1992) to treat the stochastic collision-coalescence process in clouds. Variants of Gillespie's algorithm are widely used in different fields, including simulations of gene regulatory networks (El Samad, Khammash, Petzold, & Gillespie, 2005), chemical kinetics (Gillespie, 2007), and sintering in flames (Wells, Morgan, Kraft, & Wagner, 2006).

Coagulation between aerosol particles is simulated in PartMC by generating a realization of a Poisson process with a Brownian coagulation kernel. For the large number of particles used here we cannot simply implement the Stochastic Simulation Algorithm by Gillespie (1975). Instead it is necessary to employ an efficient approximate simulation method. We developed a binned sampling method to efficiently sample from the highly multi-scale coagulation kernel (in our case the Brownian kernel) in the presence of a very non-uniform particle size distribution, which is described in detail in Riemer et al. (2009). This method uses a fixed timestep, which for this paper was taken to be 1 min.

Particle emissions and dilution with background air are also implemented in a stochastic manner. Because we are using a finite number of particles to approximate the current aerosol population, we need to add a finite number of emitted particles to the volume at each timestep. Over time these finite particle samplings should approximate the continuum emission distribution, so the samplings at each timestep must be different. Similarly to coagulation, we assume that emissions are memoryless, so that emission of each particle is uncorrelated with emission of any other particle. Under this assumption the appropriate statistics are Poisson distributed, whereby the distribution of finite particles is parametrized by the mean emission rate and distribution.

Lastly, we must also obtain a finite sampling of background particles that have diluted into our computational volume during each timestep. In addition, some of the particles in our current sample will dilute out of our volume and will be lost, so this must be sampled as well. Again, we assume that dilution is memoryless, so that dilution of each particle is uncorrelated with the dilution of any other particle or itself at other times, and that once a particle dilutes out it is lost.

We coupled the stochastic PartMC particle-resolved aerosol model to the deterministic MOSAIC gas- and aerosol-chemistry code (Zaveri, Easter, Fast, & Peters, 2008) in a time- or operator-splitting fashion (Press, Teukolsky, Vetterling, & Flannery, 2007, Section 20.3.3), using a 1 min timestep. MOSAIC treats all the globally important aerosol species including sulfate, nitrate, chloride, carbonate, ammonium, sodium, calcium, primary organic aerosol (POA), secondary organic aerosol (SOA), black carbon (BC), and inert inorganic mass.

MOSAIC consists of four computationally efficient modules: (1) the gas-phase photochemical mechanism CBM-Z (Zaveri & Peters, 1999); (2) the multicomponent Taylor expansion method (MTEM) for estimating activity coefficients of electrolytes and ions in aqueous solutions (Zaveri, Easter, & Wexler, 2005); (3) the multicomponent equilibrium solver for aerosols (MESA) for intra-particle solid–liquid partitioning (Zaveri, Easter, & Peters, 2005); and (4) the adaptive step time-split Euler method (ASTEM) for dynamic gas-particle partitioning over size- and composition-resolved aerosol (Zaveri et al., 2008). The version of MOSAIC implemented here also includes a treatment for SOA based on the SORGAM scheme (Schell, Ackermann, Binkowski, & Ebel, 2001).

3. Idealized urban plume scenario

For our urban plume scenario, we tracked the evolution of gas phase species and aerosol particles in a Lagrangian air parcel that initially contained background air and was advected over and beyond a large urban area, as described in Riemer et al. (2009). The simulation started at 06:00 local standard time (LST), and during the advection process, primary trace gases and aerosol particles from different sources were emitted into the air parcel for the duration of 12 h. After 18:00 LST, all emissions were switched off, and the evolution of the air parcel was tracked for another 12 h. The time series of temperature, relative humidity and mixing height are shown in Fig. 1.

Initial gas-phase and aerosol particle concentrations as well as gas phase and particle emissions were the same as in Riemer et al. (2009). The gas phase emissions varied throughout the emission time interval according to a typical diurnal cycle found in polluted urban areas.

The initial particle distribution, which was identical to the background aerosol distribution, was bimodal with Aitken and accumulation modes (Jaenicke, 1993). We assumed that it consisted of (NH$_4$)$_2$SO$_4$ and POA, as shown in Table 1. We considered three different types of carbonaceous aerosol emissions: (1) meat cooking aerosol, (2) diesel vehicle emissions, and (3) gasoline vehicle emissions. The parameters for the distributions of these three emission categories were based on Eldering and Cass (1996), Kittelson, Watts, and Johnson (2006), and Kittelson, Watts, Johnson, Schauer, and Lawson (2006), respectively. For simplicity in this idealized study, the particle emissions strength and their size distribution and composition were kept constant with time during the time period of emission.
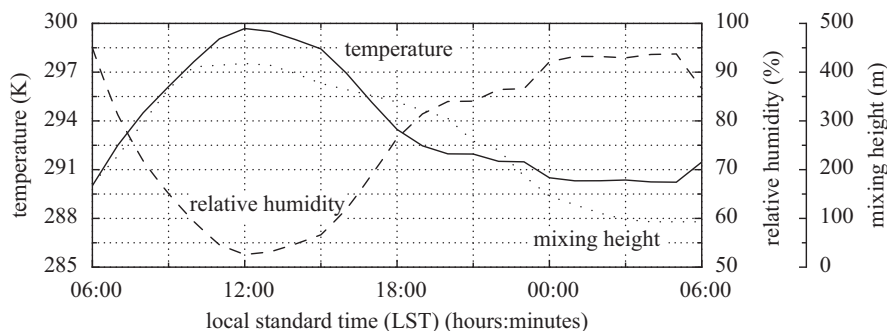
Fig. 1. Time series of temperature, relative humidity, and mixing height over the course of the 24 h simulation. The pressure and water mixing ratio were kept constant.

Table 1
Initial and emitted aerosol distribution parameters.

Initial/background	N (m^{-3})	D_{gn} (μm)	σ_g (1)	Composition by mass
Aitken mode	3.2×10^9	0.02	1.45	50% $(NH_4)_2SO_4$, 50% POA
Accumulation mode	2.9×10^9	0.116	1.65	50% $(NH_4)_2SO_4$, 50% POA
Emissions	E (m^{-2} s^{-1})	D_{gn} (μm)	σ_g (1)	Composition by mass
Meat cooking	9×10^6	0.086	1.9	100% POA
Diesel vehicles	1.6×10^8	0.05	1.7	30% POA, 70% BC
Gasoline vehicles	5×10^7	0.05	1.7	80% POA, 20% BC

The initial aerosol distribution is also used as the background aerosol distribution. The percentages for the composition are by mass. E is the area source strength of particle emissions. Dividing E by the mixing height and multiplying by a normalized composition distribution gives the number distribution emission rate.
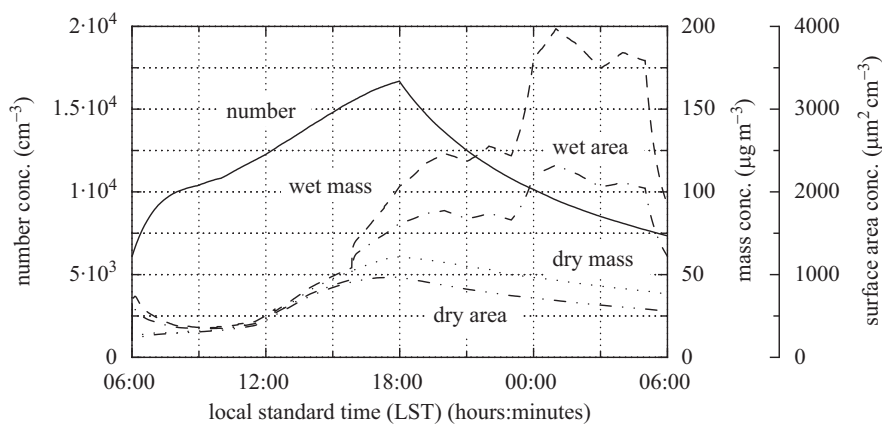

Fig. 2. Time series of bulk aerosol concentrations. Particle and gas phase emissions were present from 06:00 to 18:00 LST.

Furthermore, we assumed that every particle from a given source had the same composition, with the species listed in Table 1, since to date the mixing state of particle emissions is still not well quantified. In particular, we assume that the diesel and gasoline exhaust particles consist exclusively of POA and BC, which is very nearly the case (Andreae & Gelencśer, 2006; Kleeman et al., 2000; Medalia & Rivin, 1982). At this point we do not have quantitative information on a single-particle basis of how the mean of this ratio depends on size or what the variance around this mean is, so we assigned all diesel particles a fixed BC/POA ratio and all gasoline particles a different fixed ratio. We also neglected any trace amounts of ionic species and metals, any variations with respect to vehicle operation, and any other particle types that may be present in the exhaust. For gasoline engines we took a BC dry-mass fraction of $w_{BC,dry} = 20\%$ based on Somers (2004, p. 5) (about 20% overall) and Nam et al. (2008, Section 8.4, p. 54) (a composite figure of 17.3%). For diesel engines we used a BC dry mass fraction of $w_{BC,dry} = 70\%$, consistent with Robert, Kleeman, and Jakober (2007) (73% for ultrafine particles and 61% for fine) and Somers (2004, p. 5) (about 50–80%).

Fig. 2 gives an overview of how the total number concentration, wet and dry mass concentrations, and wet and dry surface area concentrations developed over the course of the simulation period. Total number concentration increased during the time period of emission (06:00–18:00 LST) to a maximum of 16 700 cm^{-3}, and decreased after this due to dilution. The dry mass and
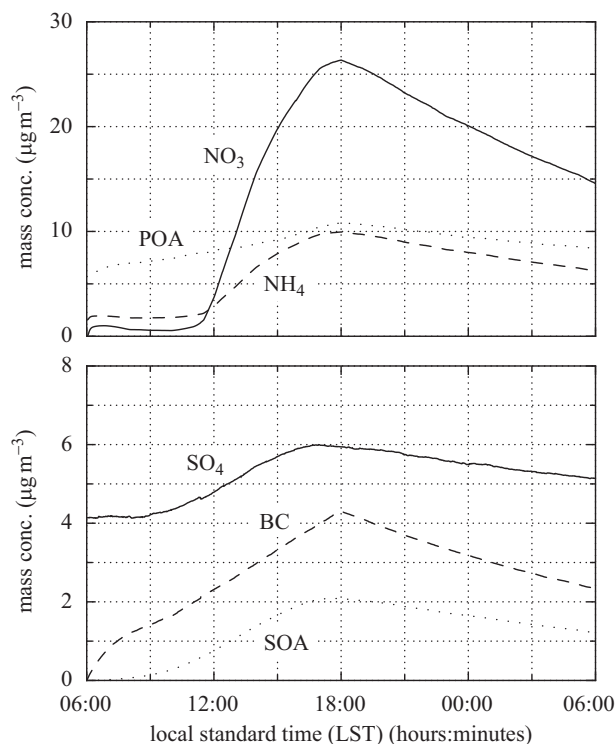
Fig. 3. Time series of mass concentrations of selected aerosol species: nitrate (NO_3), ammonium (NH_4), POA, sulfate (SO_4), BC, and SOA. Particle and gas phase emissions were present from 06:00 to 18:00 LST.

surface concentrations likewise increased during the first 12 h of simulation, both due to the primary emissions and due to the formation of inorganic and organic aerosol mass as is shown in more detail in Fig. 3. Comparing wet and dry mass and surface concentrations, we see that the particles initially contained water. As the relative humidity decreased during the morning hours (see Fig. 1), the particles became dry and stayed dry until about 16:00 LST when the relative humidity increased over 61%. By this time, the particles had accumulated large amounts of ammonium nitrate (see Fig. 1), and as a result they took up large amounts of water, especially during the following night when the relative humidity increased over 90%.

Fig. 3 shows time series of the bulk aerosol mass concentrations as they result from this urban plume scenario. We observed a pronounced production of ammonium nitrate, reaching nitrate mass concentration of up to $26 \, \mu g \, m^{-3}$ and ammonium mass concentration of $10 \, \mu g \, m^{-3}$ in the late afternoon. Sulfate mass concentrations increased from 4.1 to $6.0 \, \mu g \, m^{-3}$ due to condensation of photochemically produced sulfuric acid. POA and BC were directly emitted (with a temporally constant rate) and accumulated to 11 and $4.3 \, \mu g \, m^{-3}$, respectively, until 18:00 LST when the emissions stopped. After 18:00 LST the mass concentrations declined due to dilution, especially nitrate and BC for which the background mass concentration were zero.

3.1. Characterizing mixing state

To characterize the mixing state and to discuss the composition of a particle, we refer to the BC mass fractions as

$$w_{BC,dry} = \frac{\mu_{BC}}{\mu_{dry}}, \tag{2}$$

where μ_{BC} is the mass of BC in a given particle and μ_{dry} is the total dry mass.

Based on this quantity, we then define a two-dimensional number concentration that is a function of both particle composition and diameter. The two-dimensional cumulative number distribution $N_{BC,dry}(w, D)$ is the number of particles per volume that have a diameter less than D and a BC mass fraction of less than w. The top panels in Fig. 4 show the corresponding two-dimensional distributions after 1 h and after 24 h of simulation time. Since even at the time of emission no particles were pure BC, particles were not present at $w_{BC,dry} = 100\%$. Fresh emissions from diesel vehicles ($w_{BC,dry} = 70\%$) and gasoline vehicles ($w_{BC,dry} = 20\%$) appear as horizontal lines since particles in one emission category were all emitted with the same composition. At $w_{BC,dry} = 0\%$ all the particles appear that do not contain any BC (i.e. background particles and particles from meat cooking emissions that have not undergone coagulation with particles containing BC). After 1 h (07:00 LST) a small number of particles between these three classes indicate the occurrence of coagulation. Comparing this result to the result for the end of the simulation, we note that at the end of the simulation particles with diameter below $D = 0.03 \, \mu m$ were heavily depleted. A comparison with a simulation
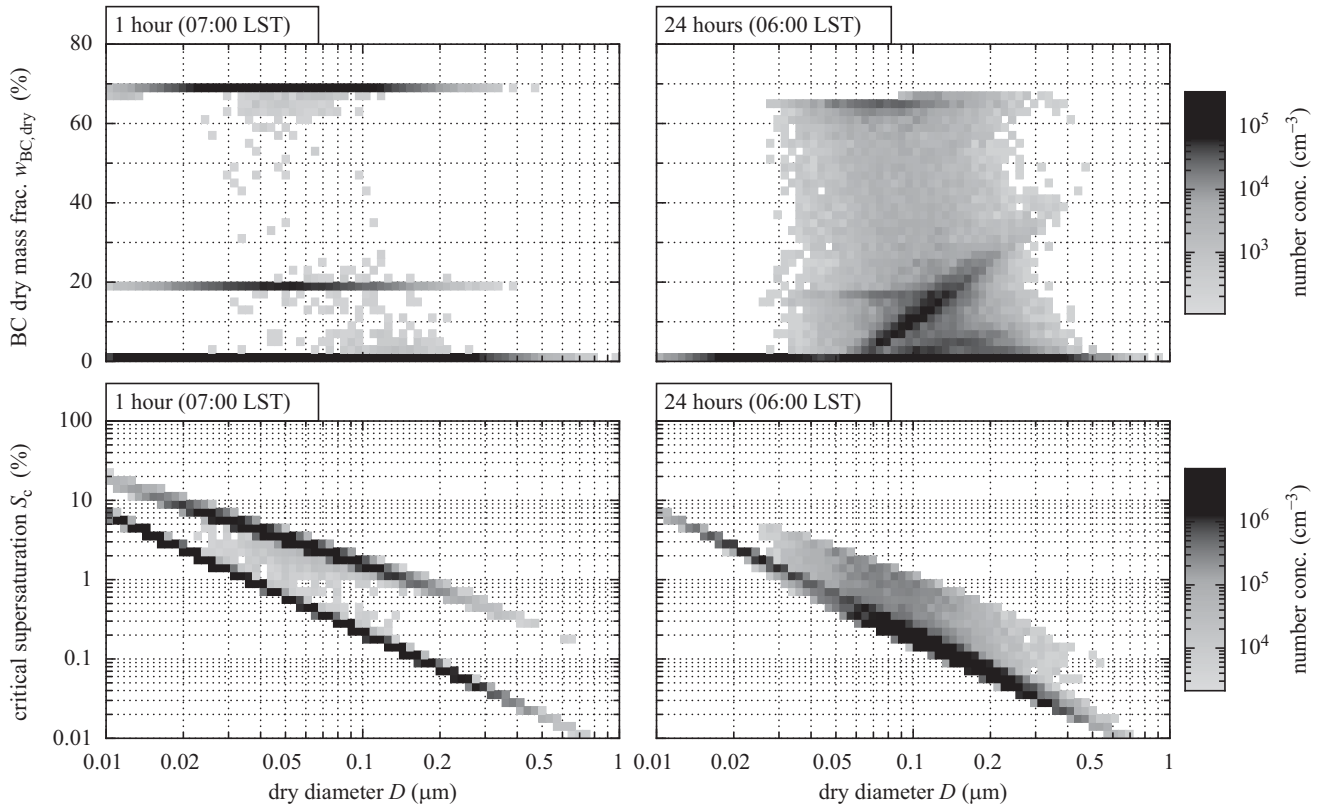
Fig. 4. Two-dimensional number distributions after 1 h (07:00 LST) and 24 h (06:00 LST the next day) of simulation. The top panels show the two-dimensional distribution $\partial^2 N_{BC,dry}(D,w)/(\partial \log_{10}D \, \partial w)$ with respect to diameter D and BC dry mass fraction $w_{BC,dry}$, while the bottom panels show the two-dimensional distribution $\partial^2 N_S(D,S_c)/(\partial \log_{10}D \, \partial \log_{10}S_c)$ with respect to diameter D and critical supersaturation S_c.

without coagulation (results not shown here) showed that this depletion can be attributed to coagulation of small particles with larger particles. A continuum of mixing states formed between the extreme mixing states of $w_{BC,dry} = 0\%$ and 70%.

3.2. Calculating CCN activity

Given that we track the composition evolution of each individual particle throughout the simulation, we can calculate the critical supersaturation S_c that the particle needs in order to activate. We use the concept of a dimensionless hygroscopicity parameter suggested by Ghan et al. (2001) or Petters and Kreidenweis (2007). In Petters and Kreidenweis (2007) this parameter is denoted by κ, and we adopt their notation for the remainder of the paper. This concept has the advantage that results from laboratory measurements can be used to quantify the hygroscopicity of complex compounds such as organic substances for which κ values cannot be calculated in a straightforward manner.

Following Petters and Kreidenweis (2007), the hygroscopicity parameter κ is defined through its effect on the water activity a_w of the solution:

$$\frac{1}{a_w} = 1 + \kappa \frac{V_{dry}}{V_w}, \tag{3}$$

where V_{dry} is the dry particle volume and V_w is the volume of water in the particle.

The saturation ratio S over an aqueous solution droplet of diameter D is given by

$$S(D) = a_w \exp\left(\frac{4\sigma_w M_w}{RT\rho_w D}\right), \tag{4}$$

where σ_w is the surface tension of the solution–air interface, M_w is the molecular weight of water, R is the universal gas constant, and T is the temperature.

Using Eq. (3), Eq. (4) can be written as

$$S(D) = \frac{D^3 - D_{dry}^3}{D^3 - D_{dry}^3(1 - \kappa)} \exp\left(\frac{A}{D}\right), \tag{5}$$

where D_{dry} is the dry diameter of the particle, which is related to V_{dry} as $V_{\mathrm{dry}} = (\pi/6)D_{\mathrm{dry}}^3$, D is the wet diameter, and $A = 4\sigma_{\mathrm{w}}M_{\mathrm{w}}/(RT\rho_{\mathrm{w}})$.

To calculate the critical supersaturation S_{c}, the critical diameter $D_{\mathrm{c}} \geqq D_{\mathrm{dry}}$ needs to be determined for which $S(D)$ becomes maximal. Taking the derivative of Eq. (5) with respect to D gives

$$\frac{\partial S(D)}{\partial D} = \frac{-Af(D)}{(D^3 - D_{\mathrm{dry}}^3(1 - \kappa))^2 D^2} \exp\left(\frac{A}{D}\right), \tag{6}$$

where $f(D)$ is given by

$$f(D) = D^6 - \frac{3D_{\mathrm{dry}}^3 \kappa}{A}D^4 - D_{\mathrm{dry}}^3(2 - \kappa)D^3 + D_{\mathrm{dry}}^6(1 - \kappa) \tag{7}$$

$$= \underbrace{\left(\left(D^3 - D_{\mathrm{dry}}^3\frac{2 - \kappa}{2}\right)^2 - D_{\mathrm{dry}}^6\frac{\kappa^2}{4}\right)}_{f_1(D)} + \underbrace{\left(-\frac{3D_{\mathrm{dry}}^3 \kappa}{A}D^4\right)}_{f_2(D)}. \tag{8}$$

The denominator in (6) is positive for all $D > D_{\mathrm{dry}}$, so to find the maximum of $S(D)$ we need only solve $f(D_{\mathrm{c}}) = 0$. We note that $f_1(D)$ is quadratic in D^3 with roots at $(1 - \kappa)^{1/3}D_{\mathrm{dry}}$ and D_{dry}, while $f_2(D)$ is always negative. Thus from (8) we see that $f(D)$ has exactly one root greater than D_{dry}. We solve $f(D_{\mathrm{c}}) = 0$ for the critical diameter D_{c} using Brent's method (see Brent, 2002, Chapter 4; Press et al., 2007, Section 9.2.1). Using D_{c} in Eq. (5) gives the critical supersaturation S_{c}.

The overall κ for a particle is the volume-weighted average of the κ values of the constituent species. This requires the assignment of individual κ values for each aerosol component in MOSAIC. Petters and Kreidenweis (2007) compiled a table (Table 1 in their paper) with κ values for a variety of inorganic and organic species based on recent laboratory measurements or on thermodynamic model calculations. For $(NH_4)_2SO_4$ and NH_4NO_3 they report κ values of 0.61 and 0.67, based on calculations by Clegg, Brimblecombe, and Wexler (1998) and measurements by Svenningsson et al. (2006), respectively. Based on this we assume $\kappa = 0.65$ for all salts formed from the $NH_4^+ - SO_4^{2-} - NO_3^-$ system. For all MOSAIC model species that represent SOA we assume $\kappa = 0.1$, based on measurements by Prenni, Petters, Kreidenweis, DeMott, and Ziemann (2007). Following Petters et al. (2006) we assume $\kappa = 0.001$ for POA and $\kappa = 0$ for BC.

Similarly to the use of $w_{\mathrm{BC,dry}}$ above, we can use S_{c} to define a two-dimensional cumulative number distribution $N_S(D, S_{\mathrm{c}})$ in terms of size and critical supersaturation. The bottom panels in Fig. 4 show examples of the corresponding two-dimensional distributions after 1 h (left) and after 24 h (right) of simulation. While freshly emitted diesel, gasoline and meat cooking particles differed in their BC and POA mass fractions, they were very similar in their hygroscopicity with initial κ values close to zero. After 1 h they were visible as the dark band of high number concentrations at high S_{c} values. Separated from this we see another dark band representing the most hygroscopic particles, consisting of background particles. They contain the largest fraction of inorganic mass (ammonium, sulfate, and nitrate), hence their critical supersaturation was lowest at a given size compared to the other particle types.

The individual bands are not completely separated at 1 h (bottom-left panel), but the region in between has started to fill in. The reason for this is the occurrence of coagulation, which produces particles of intermediate composition and hence corresponding intermediate S_{c} values. After 24 h the population as a whole has moved to lower critical supersaturations, and the distribution with respect to S_{c} has become more continuous (bottom-right panel). Given a certain size, the critical supersaturation ranges over about one order of magnitude. We can still identify a band of particles at the same position as in the plot for 07:00 LST. These are relatively fresh background particles that have been added to the air parcel within the last 6 h due to dilution with background air. On the other hand the particles below this band are background particles that have been in the air parcel for longer times and have therefore aged accordingly.

Fig. 5 shows CCN properties as more traditional CCN spectra. This representation is the one-dimensional projection of the bottom panels of Fig. 4 onto the critical supersaturation axis, plotted as a cumulative distribution. The change in CCN properties over the course of 24 h is obvious. After 1 h a supersaturation of about $S = 1.8\%$ is necessary to activate 50% of the particles by number. This required supersaturation decreases to about $S = 0.18\%$ after 24 h. In the following section we use the results of this urban plume scenario as a basis for estimating the aging time-scales.

4. First-order models of aging

In this section we describe the first-order model of black carbon aging for which we use the particle-resolved data simulated with PartMC-MOSAIC, in order to determine the aging time-scale. We emphasize that we do not actually simulate using the first-order models presented in this section. Such first-order systems are frequently used, however, to model the conversion from hydrophobic to hydrophilic black carbon with the single parameter of aging rate or its inverse, the aging time-scale τ (Croft et al., 2005). More specifically, the aging time-scale represents the time-scale on which BC-containing particles that would initially not activate turn into particles that can be activated, given a certain chosen supersaturation threshold. Budget equations for the fresh and aged populations can be formulated in terms of either number or mass. A number based aging time-scale is relevant for aerosol indirect forcing as the cloud optical properties depend on the cloud droplet number distribution. On the other hand,
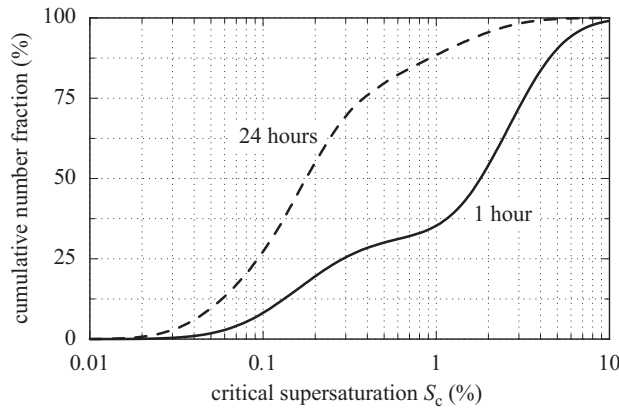
Fig. 5. Cloud condensation nuclei spectra after 1 h (07:00 LST) and 24 h (06:00 LST the next day) of simulation based on the simulation results shown in Fig. 4.

a mass aging time-scale is relevant for in-cloud scavenging and wet removal of BC mass. In the following we will present results for both number- and mass-based aging time-scales.

At time t, the total number concentration $N_{BC}(t)$ of BC-particles is the sum of the number concentration of BC-containing fresh particles $N_f(t)$ and the number concentration of BC-containing aged particles $N_a(t)$. We define analogously the total BC mass concentration $M_{BC}(t)$, the BC mass concentration in fresh BC-containing particles $M_f(t)$, and the BC mass concentration in aged BC-containing particles $M_a(t)$. The aged and fresh populations are separated by applying an aging criterion, in our case activation at a certain supersaturation threshold S_c. Fresh particles are those with critical supersaturation above the threshold value, while aged particles have critical supersaturations below the threshold.

In the PartMC model we explicitly track a finite number of particles in a computational volume V. The number of fresh and aged BC-containing particles in the volume $V(t_k)$ at time t_k is denoted by $n_f(t_k)$ and $n_a(t_k)$, respectively. Similarly, $m_f(t_k)$ and $m_a(t_k)$ are, respectively, the total mass of BC in fresh and aged BC-containing particles in $V(t_k)$. The number and mass concentrations of fresh BC-containing particles in $V(t_k)$ are then given by

$$
\begin{aligned}
N_f(t_k) &= \frac{n_f(t_k)}{V(t_k)}, \quad M_f(t_k) = \frac{m_f(t_k)}{V(t_k)}, \\
N_a(t_k) &= \frac{n_a(t_k)}{V(t_k)}, \quad M_a(t_k) = \frac{m_a(t_k)}{V(t_k)}.
\end{aligned}
\tag{9}
$$

The fresh and aged number and mass concentrations can change due to emission and dilution, while condensation/evaporation and coagulation can transfer number and mass concentration from the fresh to the aged population and vice versa. Condensation/evaporation and coagulation can also change number and mass concentrations without transferring number.

Changes in number and mass concentrations also occur due to temperature and pressure changes. In our model we neglect at present the impact of heterogeneous reactions on the surface of the particles, although studies have shown that these also contribute to the aging process (Rudich, Donahue, & Mentel, 2007). The gain and loss terms for the fresh and aged BC-containing populations are given in Table 2.

To express changes in number and mass for coagulation we consider that all constituent particles are lost during a coagulation event and the product of coagulation is a gain of a new particle. Table 3 shows the overview of all possible combinations and the resulting terms for each of those combinations. For example, let us assume that there are four independent coagulation events within a single timestep: one event between two fresh BC-containing particles resulting in an aged particle (one event of type E2), two events between fresh and aged BC-containing particles each resulting in an aged particle (two events of type E4), and one event between a fresh BC-containing particle and a non-BC-containing particle resulting in a fresh particle (one event of type E6). Adding the gain and loss terms for the various events gives total losses of $\Delta n_{f\to a}^{coag}(t_{k-1}, t_k) = 4$, $\Delta n_{a\to a}^{coag}(t_{k-1}, t_k) = 2$, and $\Delta n_{f\to f}^{coag}(t_{k-1}, t_k) = 1$, while the total gains are $\Delta n_f^{coag}(t_{k-1}, t_k) = 1$ and $\Delta n_a^{coag}(t_{k-1}, t_k) = 3$. In this example the number of fresh BC-containing particles n_f decreases by four, and the number of aged BC-containing particles n_a increases by one, as can also be seen by adding the terms in Eqs. (20) and (21) below.

Note that for each particle pairing in Table 3 there can be two outcomes. For example, coagulation of a small fresh and large aged particle generally produces an aged particle, while coagulation of large fresh and small aged generally produces a fresh particle. When S_c, as calculated in Eqs. (5) and (6), is used as the criterion for fresh versus aged, it can be shown that coagulation of two aged particles never produces a fresh particle, and that the coagulation of two fresh particles with S_c values close to the cutoff value can produce an aged particle.

Table 2
Description of individual terms in Eqs. (14) and (15).

Terms	Description
$N_f(t), N_a(t)$	Number concentration of fresh/aged BC-containing particles
$\dot{N}_f^{emit}(t), \dot{N}_a^{emit}(t)$	Gain rate of number concentration of fresh/aged BC-containing particles due to emissions and dilution into the air parcel
$\dot{N}_f^{dilution}(t), \dot{N}_a^{dilution}(t)$	Loss rate of number concentration of fresh/aged BC-containing particles due to dilution out of the air parcel
$\dot{N}_{f\to a}^{cond}(t), \dot{N}_{a\to f}^{cond}(t)$	Gain rate of number concentration of aged/fresh BC-containing particles due to condensation or evaporation on fresh/aged particles
$\dot{N}_f^{coag}(t), \dot{N}_a^{coag}(t)$	Gain rate of number concentration of fresh/aged BC-containing particles from coagulation events
$\dot{N}_{f\to f}^{coag}(t), \dot{N}_{f\to a}^{coag}(t)$	Loss rate of number concentration of fresh BC-containing particles to coagulation events resulting in fresh/aged particles
$\dot{N}_{a\to a}^{coag}(t), \dot{N}_{a\to f}^{coag}(t)$	Loss rate of number concentration of aged BC-containing particles to coagulation events resulting in aged/fresh particles
$\dot{N}_f^{density}(t), \dot{N}_a^{density}(t)$	Gain rate of number concentration of fresh/aged BC-containing particles due to air density changes
$\dot{N}^{aging}(t), \dot{N}^{de-aging}(t)$	Net transfer rate of fresh-to-aged/aged-to-fresh number concentration of BC-containing particles

With the exception of $\dot{N}_f^{density}(t)$ and $\dot{N}_a^{density}(t)$ all of these terms must be non-negative. The same notation is for the terms in Eqs. (16) and (17) for mass concentration, and for the corresponding discrete Eqs. (20)–(23). The discrete terms are expressed as a change in number or mass within a timestep, so that $\Delta n_{f\to a}^{cond}(t_{k-1}, t_k)$ is the number of BC-containing particles in the computational volume that change from fresh to aged due only to condensation during the timestep from time t_{k-1} to t_k, for example. There are no discrete terms for air density changes as they are incorporated by changing the computational volume V.

Table 3
The different coagulation events and the resulting expressions for the loss and gain terms of the number of fresh and aged BC-containing particles.

Event type	Particle 1	Particle 2	Resulting particle	Non-zero loss terms	Non-zero gain terms
E1	Fresh	Fresh	Fresh	$\Delta n_{f\to f}^{coag} = 2$	$\Delta n_f^{coag} = 1$
E2	Fresh	Fresh	Aged	$\Delta n_{f\to a}^{coag} = 2$	$\Delta n_a^{coag} = 1$
E3	Aged	Fresh	Fresh	$\Delta n_{a\to f}^{coag} = 1, \Delta n_{f\to f}^{coag} = 1$	$\Delta n_f^{coag} = 1$
E4	Aged	Fresh	Aged	$\Delta n_{a\to a}^{coag} = 1, \Delta n_{f\to a}^{coag} = 1$	$\Delta n_a^{coag} = 1$
E5	Aged	Aged	Aged	$\Delta n_{a\to a}^{coag} = 2$	$\Delta n_a^{coag} = 1$
E6	Fresh	Non-BC	Fresh	$\Delta n_{f\to f}^{coag} = 1$	$\Delta n_f^{coag} = 1$
E7	Fresh	Non-BC	Aged	$\Delta n_{f\to a}^{coag} = 1$	$\Delta n_a^{coag} = 1$
E8	Aged	Non-BC	Fresh	$\Delta n_{a\to f}^{coag} = 1$	$\Delta n_f^{coag} = 1$
E9	Aged	Non-BC	Aged	$\Delta n_{a\to a}^{coag} = 1$	$\Delta n_a^{coag} = 1$

Similar expressions exist for mass changes Δm in the particle-resolved model and for the number rates $\dot{N}$ and mass rates $\dot{M}$ in the continuous model.

Coagulation can result in a net loss of number but must conserve mass. We thus have

$$\dot{N}_a^{coag}(t) \le \dot{N}_{f\to a}^{coag}(t) + \dot{N}_{a\to a}^{coag}(t), \tag{10}$$

$$\dot{M}_a^{coag}(t) = \dot{M}_{f\to a}^{coag}(t) + \dot{M}_{a\to a}^{coag}(t), \tag{11}$$

$$\Delta n_a^{coag}(t_{k-1}, t_k) \le \Delta n_{f\to a}^{coag}(t_{k-1}, t_k) + \Delta n_{a\to a}^{coag}(t_{k-1}, t_k), \tag{12}$$

$$\Delta m_a^{coag}(t_{k-1}, t_k) = \Delta m_{f\to a}^{coag}(t_{k-1}, t_k) + \Delta m_{a\to a}^{coag}(t_{k-1}, t_k) \tag{13}$$

and similarly for coagulation resulting in fresh particles.

The following continuous equations describe the evolution of the number and mass concentrations of fresh and aged BC-containing populations:

$$\frac{dN_f(t)}{dt} = \dot{N}_f^{density}(t) + \dot{N}_f^{emit}(t) - \dot{N}_f^{dilution}(t) + \dot{N}_{a\to f}^{cond}(t) + \dot{N}_f^{coag}(t) - \dot{N}_{f\to f}^{coag}(t) - \underbrace{(\dot{N}_{f\to a}^{cond}(t) + \dot{N}_{f\to a}^{coag}(t))}_{\dot{N}^{aging}(t)}, \tag{14}$$

$$\frac{dN_a(t)}{dt} = \dot{N}_a^{density}(t) + \dot{N}_a^{emit}(t) - \dot{N}_a^{dilution}(t) + \dot{N}_{f\to a}^{cond}(t) + \dot{N}_a^{coag}(t) - \dot{N}_{a\to a}^{coag}(t) - \underbrace{(\dot{N}_{a\to f}^{cond}(t) + \dot{N}_{a\to f}^{coag}(t))}_{\dot{N}^{de-aging}(t)}, \tag{15}$$

$$\frac{dM_f(t)}{dt} = \dot{M}_f^{\text{density}}(t) + \dot{M}_f^{\text{emit}}(t) - \dot{M}_f^{\text{dilution}}(t) + \underbrace{(\dot{M}_{a\to f}^{\text{cond}}(t) + \dot{M}_{a\to f}^{\text{coag}}(t))}_{\dot{M}^{\text{de-aging}}(t)} - \underbrace{(\dot{M}_{f\to a}^{\text{cond}}(t) + \dot{M}_{f\to a}^{\text{coag}}(t))}_{\dot{M}^{\text{aging}}(t)},$$
(16)

$$\frac{dM_a(t)}{dt} = \dot{M}_a^{\text{density}}(t) + \dot{M}_a^{\text{emit}}(t) - \dot{M}_a^{\text{dilution}}(t) + \underbrace{(\dot{M}_{f\to a}^{\text{cond}}(t) + \dot{M}_{f\to a}^{\text{coag}}(t))}_{\dot{M}^{\text{aging}}(t)} - \underbrace{(\dot{M}_{a\to f}^{\text{cond}}(t) + \dot{M}_{a\to f}^{\text{coag}}(t))}_{\dot{M}^{\text{de-aging}}(t)}.$$
(17)

Note that the mass Eqs. (16) and (17) have been simplified from forms identical to the number Eqs. (14) and (15) by using Eq. (11) for the conservation of mass during coagulation. Condensation (or rather evaporation) and coagulation can in principle also produce a transfer from aged to fresh particles. This is reflected by the terms denoted as $\dot{N}^{\text{de-aging}}(t)$ and $\dot{M}^{\text{de-aging}}(t)$ above.

The aging time-scales τ_N and τ_M for number and mass are then determined by the first-order models:

$$\dot{N}^{\text{aging}}(t) = \frac{1}{\tau_N(t)} N_f(t),$$
(18)

$$\dot{M}^{\text{aging}}(t) = \frac{1}{\tau_M(t)} M_f(t).$$
(19)

The discrete versions of the balance Eqs. (14)–(17) are

$$n_f(t_k) - n_f(t_{k-1}) = \Delta n_f^{\text{emit}}(t_{k-1}, t_k) - \Delta n_f^{\text{dilution}}(t_{k-1}, t_k) + \Delta n_{a\to f}^{\text{cond}}(t_{k-1}, t_k) + \Delta n_f^{\text{coag}}(t_{k-1}, t_k) - \Delta n_{f\to f}^{\text{coag}}(t_{k-1}, t_k)$$
$$- \underbrace{(\Delta n_{f\to a}^{\text{cond}}(t_{k-1}, t_k) + \Delta n_{f\to a}^{\text{coag}}(t_{k-1}, t_k))}_{\Delta n^{\text{aging}}(t_{k-1}, t_k)},$$
(20)

$$n_a(t_k) - n_a(t_{k-1}) = \Delta n_a^{\text{emit}}(t_{k-1}, t_k) - \Delta n_a^{\text{dilution}}(t_{k-1}, t_k) + \Delta n_{f\to a}^{\text{cond}}(t_{k-1}, t_k) + \Delta n_a^{\text{coag}}(t_{k-1}, t_k) - \Delta n_{a\to a}^{\text{coag}}(t_{k-1}, t_k)$$
$$- \underbrace{(\Delta n_{a\to f}^{\text{cond}}(t_{k-1}, t_k) + \Delta n_{a\to f}^{\text{coag}}(t_{k-1}, t_k))}_{\Delta n^{\text{de-aging}}(t_{k-1}, t_k)},$$
(21)

$$m_f(t_k) - m_f(t_{k-1}) = \Delta m_f^{\text{emit}}(t_{k-1}, t_k) - \Delta m_f^{\text{dilution}}(t_{k-1}, t_k) + \underbrace{(\Delta m_{a\to f}^{\text{cond}}(t_{k-1}, t_k) + \Delta m_{a\to f}^{\text{coag}}(t_{k-1}, t_k))}_{\Delta m^{\text{de-aging}}(t_{k-1}, t_k)}$$
$$- \underbrace{(\Delta m_{f\to a}^{\text{cond}}(t_{k-1}, t_k) + \Delta m_{f\to a}^{\text{coag}}(t_{k-1}, t_k))}_{\Delta m^{\text{aging}}(t_{k-1}, t_k)},$$
(22)

$$m_a(t_k) - m_a(t_{k-1}) = \Delta m_a^{\text{emit}}(t_{k-1}, t_k) - \Delta m_a^{\text{dilution}}(t_{k-1}, t_k) + \underbrace{(\Delta m_{f\to a}^{\text{cond}}(t_{k-1}, t_k) + \Delta m_{f\to a}^{\text{coag}}(t_{k-1}, t_k))}_{\Delta m^{\text{aging}}(t_{k-1}, t_k)}$$
$$- \underbrace{(\Delta m_{a\to f}^{\text{cond}}(t_{k-1}, t_k) + \Delta m_{a\to f}^{\text{coag}}(t_{k-1}, t_k))}_{\Delta m^{\text{de-aging}}(t_{k-1}, t_k)}.$$
(23)

Here Eq. (13) for the discrete conservation of mass during coagulation was used to simplify the mass equations, as in the continuous case. There are no discrete terms for air density changes as they are incorporated by changing the computational volume V.

By comparing the continuous Eqs. (14)–(17) to the discrete Eqs. (20)–(23) using the relationships (9) we see that the continuous aging terms can be approximated by

$$\dot{N}^{\text{aging}}(t_k) \approx \frac{\Delta n^{\text{aging}}(t_{k-1}, t_k)}{(t_k - t_{k-1})V(t_k)},$$
(24)

$$\dot{M}^{\text{aging}}(t_k) \approx \frac{\Delta m^{\text{aging}}(t_{k-1}, t_k)}{(t_k - t_{k-1})V(t_k)},$$
(25)

where the use of V at time t_k is because the computational volume V is updated first within each timestep in the PartMC algorithm (Riemer et al., 2009, Section 3.4).

From Eqs. (18) and (19) and the relationships (9), the aging time-scales τ_N and τ_M are then approximated by

$$\tau_N(t_k) \approx \frac{(t_k - t_{k-1})n_f(t_k)}{\Delta n^{\text{aging}}(t_{k-1}, t_k)},$$
(26)

$$\tau_M(t_k) \approx \frac{(t_k - t_{k-1})m_f(t_k)}{\Delta m^{\text{aging}}(t_{k-1}, t_k)}.$$
(27)

As we see in Section 5, the number of simulated particles that aged within each 1 min PartMC-MOSAIC timestep fluctuated significantly from timestep to timestep. For this reason we also computed aging time-scales from transfer rates ($\Delta n_{f \to a}^{cond}(t_{k-1}, t_k)$, etc.) smoothed by a Hann filter with a window width of 1 h. This did not introduce a significant error in the processed results, as can be seen from the smoothed rates in Fig. 8 and the resulting timescales in Fig. 7.

For the analysis in Section 5 we additionally define the aging time-scale τ_N^{cond} ignoring the impact of coagulation, an average time-scale $\tau_{N,day}$ during the day, and an average time-scale $\tau_{N,night}$ during the night, given by

$$\tau_N^{cond}(t_k) \approx \frac{(t_k - t_{k-1})n_f(t_k)}{\Delta n_{f \to a}^{cond}(t_{k-1}, t_k)}, \tag{28}$$

$$(\tau_{N,day})^{-1} = \frac{1}{3\,h} \int_{12:00\ LST}^{15:00\ LST} (\tau_N(t))^{-1}\, dt, \tag{29}$$

$$(\tau_{N,night})^{-1} = \frac{1}{10\,h} \int_{18:00\ LST}^{04:00\ LST} (\tau_N(t))^{-1}\, dt, \tag{30}$$

and similarly for τ_M^{cond}, $\tau_{M,day}$, $\tau_{M,night}$, $\tau_{N,day}^{cond}$, and so on.

It should be pointed out that the time-scales as defined in Eqs. (26) and (27) represent "instantaneous" time-scales for the entire BC-containing particle population, i.e. they do not take into account the history of the particles and they do not differentiate the time-scale on the basis of particle size. We chose to focus on these bulk instantaneous time-scales because they are one of the simplest and most widely implemented aging characterizations in production simulations.

To illustrate the instantaneous nature of the first-order aging model described here, let us assume conditions where the formation rate of condensable inorganics is constant and particle concentrations are low enough that coagulation is negligible. As the BC-containing particles grow by condensation, initially none of the BC particles are reaching lower critical supersaturations (e.g. 0.1%) and the instantaneous aging time-scales are very long. However, after sufficient growth has taken place, they will all reach this supersaturation at close to the same time and the instantaneous aging time-scales become very low.

To illustrate the size-dependent nature of particle aging, we need only consider that the processes that age particles (condensation and coagulation) are size dependent, so aging time-scales will vary with particle size. As discussed in Section 5, comparing τ_N and τ_M provides some information on the size-dependence of aging, since τ_M is more influenced by the aging of larger particles than is τ_N.

The particle-resolved nature of PartMC-MOSAIC gives full access to per-particle aging processes, so while in this paper we only derive instantaneous, bulk aging time-scales, it would be possible to determine the appropriate time-scales on either an individual particle basis, or by size class, or any other criterion.

5. Results

In this section we show results for supersaturation thresholds ranging between $S_c = 0.1\%$ and 0.6%. This range is consistent with the highly polluted conditions of the urban plume scenario given a typical range of updraft velocities from $0.2-0.5\,\mathrm{m\,s^{-1}}$ (stratus clouds) to $2-5\,\mathrm{m\,s^{-1}}$ (convective clouds). To limit the number of figures we use $S_c = 0.3\%$ as a base case. Fig. 6 shows the time series for N_f, N_a, and $N_{BC} = N_f + N_a$ for $S_c = 0.3\%$. Similarly to Fig. 2 where we showed the total number concentration of all particles, the total number concentration N_{BC} of BC-containing particles increased until 18:00 LST due to the diesel and gasoline emissions. After the emissions stopped, N_{BC} decreased as a result of continued dilution and coagulation. The time series
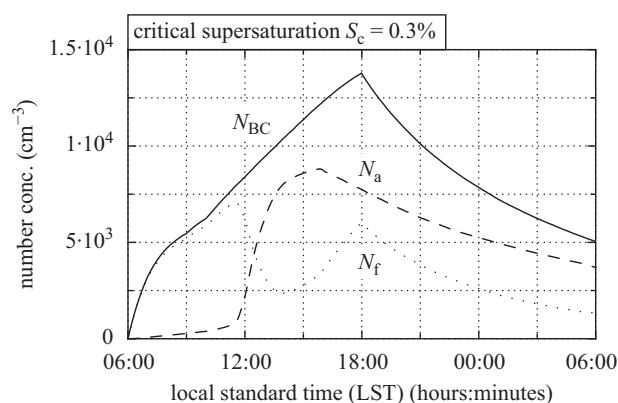
Fig. 6. Time series of total number concentration N_{BC} of BC-containing particles and number concentrations N_f and N_a for fresh and aged BC-containing particles, respectively. The critical supersaturation separating fresh and aged particles is set to $S_c = 0.3\%$.
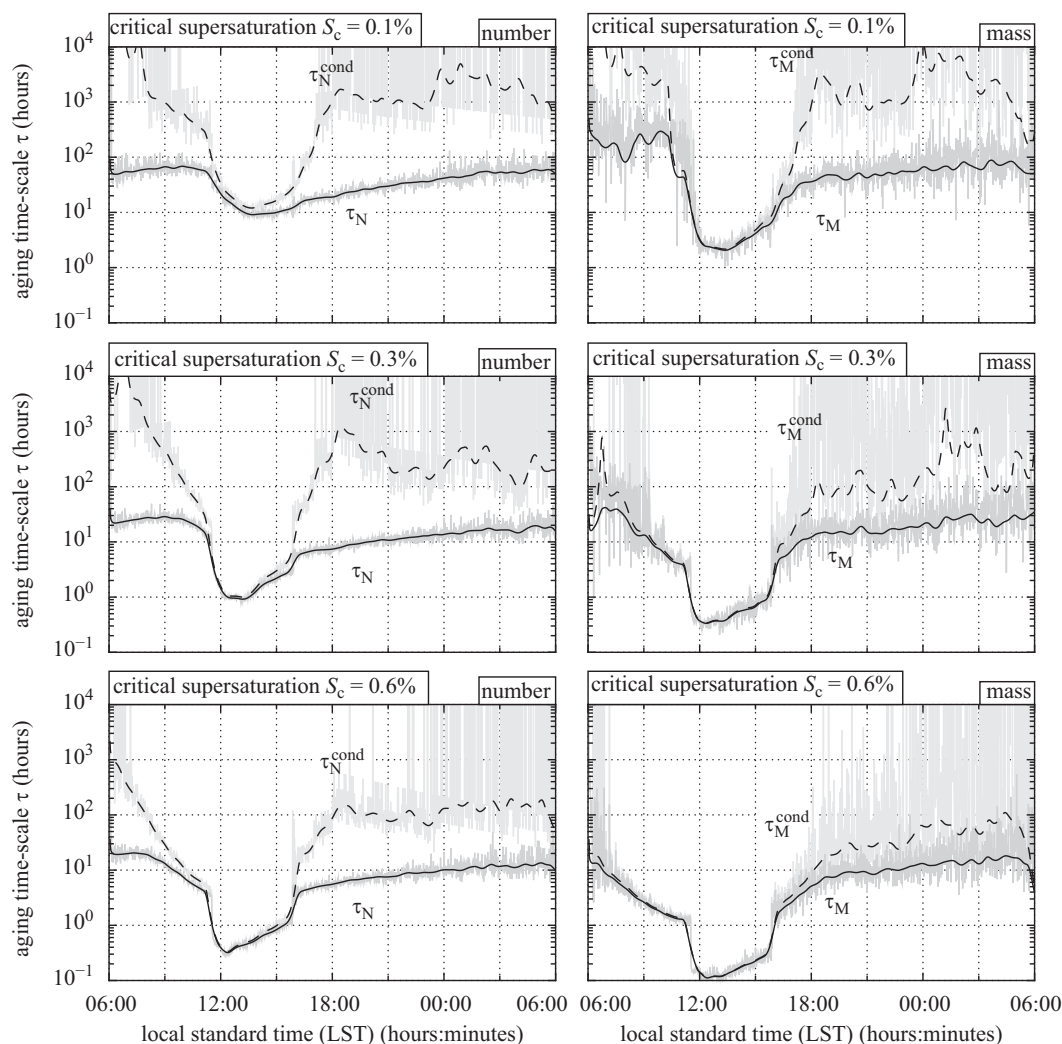
Fig. 7. Comparison of aging time-scales based on number (left) and mass (right), showing both the time-scales due to condensation and coagulation (τ_N and τ_M) and the time-scales due to condensation alone (τ_N^{cond} and τ_M^{cond}). The top panels have the critical supersaturation separating fresh from aged particles set to $S_c = 0.1\%$, while the middle panels have $S_c = 0.3\%$, and the bottom panels have $S_c = 0.6\%$.

for N_f and N_a show that both increased in the morning hours. A pronounced transfer from fresh to aged occurred after 11:30 LST, the time when nitrate formation started taking place on the dry particles (compare Fig. 3). This process efficiently contributed to the conversion of fresh particles to aged particles, which will be reflected by a short aging time-scale.

The left column of Fig. 7 compares the aging time-scales τ_N and τ_N^{cond} computed according to Eqs. (26) and (28) for different supersaturation thresholds. The top, middle and bottom panels shows the results for supersaturation thresholds $S_c = 0.1\%$, 0.3%, and 0.6%, respectively. The grey shading is the raw data, and the black lines are results computed from smoothing the transfer rates with a Hann filter with a window width of 1 h.

The solid lines represent τ_N, including the contributions due to both coagulation and condensation/evaporation according to Eq. (26). For the base case $S_c = 0.3\%$, τ_N started off in the morning with values of about 20 h. It decreased sharply after 11:00 LST, which is the time when photochemistry was at its peak, and nitrate formation was most pronounced, hence leading to a fast aging process. Between 12:00 LST and 14:00 LST, τ_N was approximately 1 h. After 16:00 LST, as photochemistry slowed down, τ_N increased again, reaching a plateau of about 15 h during the evening and night.

The broken lines represent τ_N^{cond} as defined in Eq. (28), i.e. the contribution due to coagulation is ignored. There was only a small difference between τ_N and τ_N^{cond} during midday and early afternoon when condensation was operating very effectively. However, during morning, afternoon and night, neglecting coagulation lead to larger time-scales (up to two orders of magnitude).

A similar pattern was found for $S_c = 0.6\%$, shown in the bottom panel. For this case, during the day, the aging time-scales were as low as 0.3 h. For $S_c = 0.1\%$ we generally obtained larger aging time-scales. During the morning, τ_N was about 50 h and decreased to 8 h in the early afternoon. Obviously, at $S_c = 0.1\%$, even after the growth due to condensation of ammonium nitrate, the particles were still too small to be activated to the same extent as seen for the larger supersaturations. During the following
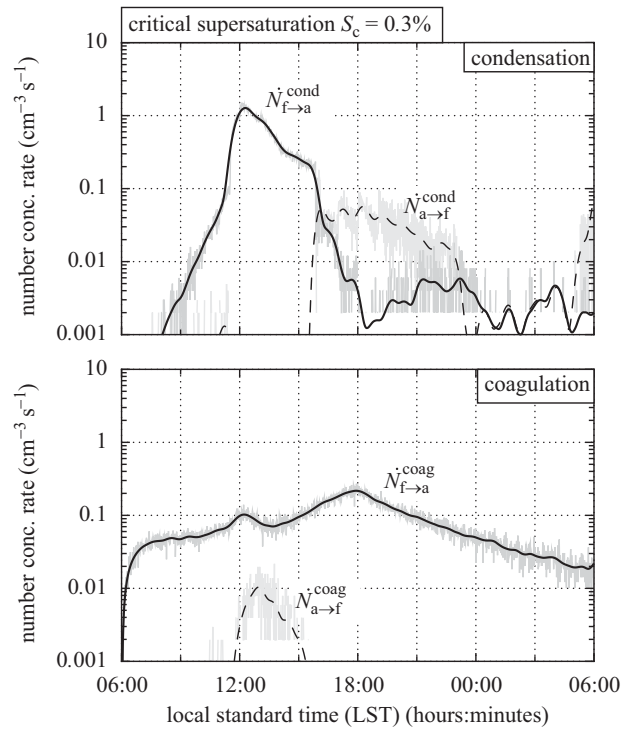
Fig. 8. Transfer rates due to condensation (top) and coagulation (bottom). The critical supersaturation separating fresh and aged particles is set to $S_c = 0.3\%$. The notation is according to Table 2.
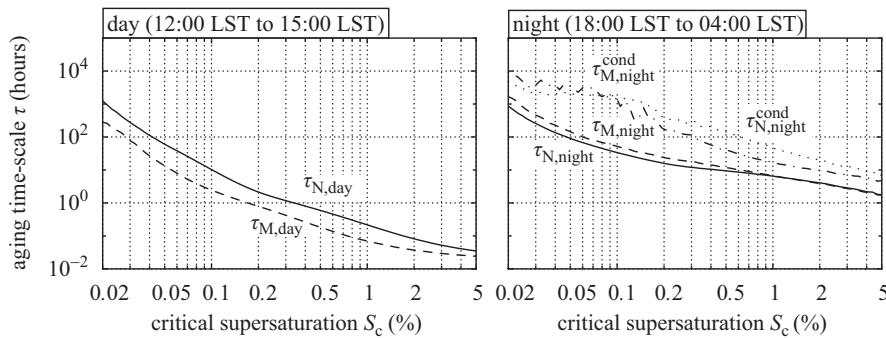

Fig. 9. Day (left) and night (right) averages of the aging time-scale, as defined in Eqs. (28)–(30). As can be see from Fig. 7, during the day the condensation-induced aging dominates, so $\tau_{N,day}^{cond}$ is almost indistinguishable from $\tau_{N,day}$, and similarly for mass.

night τ_N was around 50 h. For this low supersaturation the contrast between day and night was not as pronounced as for $S_c = 0.3\%$ or 0.6%.

Qualitatively, the temporal evolution of τ_M (right column) was similar to the number-based result τ_N. However the day/night contrast was more pronounced for the case with $S_c = 0.1\%$. Generally, we see that for the three supersaturation thresholds the time-scales based on mass during the day were about a factor of 3–4 lower than the ones based on number.

Fig. 8 shows the individual transfer terms of BC-containing particles for the case $S_c = 0.3\%$. The transfer rate $\dot{N}_{a\to f}^{coag}$ due to coagulation from aged to fresh was very small throughout the whole day, remaining below 0.01 cm^{-3} s^{-1}. The transfer rate $\dot{N}_{f\to a}^{coag}$ due to coagulation from fresh to aged followed the time series of N_f in Fig. 6. The minimum of N_f during the early afternoon was reflected in a minimum of the transfer rate $\dot{N}_{f\to a}^{coag}$. The transfer rate $\dot{N}_{f\to a}^{cond}$ due to condensation from fresh to aged was large between 11:30 and 15:00 LST, consistent with the decrease of τ_N in Fig. 7. Lastly, there was a non-zero transfer $\dot{N}_{a\to f}^{cond}$ from aged to fresh due to condensation, which was larger than $\dot{N}_{f\to a}^{cond}$ between 16:00 and 23:00 LST and after 05:00 LST of the next morning. This is due to evaporation of ammonium nitrate as the particles equilibrate with the environmental conditions.

Fig. 9 summarizes the results for the different aging time-scale definitions. We calculated $\tau_{N,day}$ and $\tau_{N,night}$ according to Eqs. (29) and (30) for several hundred different supersaturation thresholds between $S_c = 0.01\%$ and 10%, and similarly for mass.

We also distinguished between the definitions of τ including the transfer due to coagulation and condensation (solid and dashed lines), and including only the transfer due to condensation, $\tau_{N,night}^{cond}$ and $\tau_{M,night}^{cond}$ (dotted and dash-dotted lines).

As seen in both Figs. 9 and 7, the mass-based aging time-scale τ_M is smaller than the number-based aging time-scale τ_N during the day. This reflects the size-dependence of aging by condensation. Simply put, larger particles age more rapidly, and τ_M is more influenced by the aging of larger particles than is τ_N. Consider two diesel exhaust particles with initial dry diameters of 0.02 and 0.20 μm. To become a CCN at 0.3% supersaturation, 0.30 and 0.28 fg of NH_4NO_3 must condense on the particles, respectively. The larger particle requires slightly less NH_4NO_3 and its initial surface area is 100 times that of the smaller particle, so the larger particle will grow to a CCN with critical supersaturation of 0.3% first.

During the night the above pattern is reversed, with the aging dominated by coagulation of fresh particles with aged or background particles. Coagulation is more rapid for the smaller fresh particles, and τ_N is more influenced by the aging of these smaller particles, leading to number-based aging time-scales τ_N smaller than the mass-based aging time-scales τ_M during the night.

For this particular urban plume scenario the following general features emerge: during the day, condensation of semi-volatile species, in our case especially ammonium nitrate, was the dominant process for aging. The time-scales based on number were larger than the time-scales based on mass during the day, by roughly a factor of three. The aging time-scales had a strong dependence on supersaturation threshold. For example for $S_c = 0.1\%$, $\tau_{N,day}$ was 11 h, whereas for $S_c = 0.6\%$, $\tau_{N,day}$ was only 0.47 h. During the night condensation was limited, hence coagulation was the dominant aging process. For low supersaturation thresholds, the time-scales based on number were smaller than the time-scales based on mass, but this difference decreased for higher supersaturation thresholds.

6. Conclusions

In this paper we presented a method for explicitly calculating aging time-scales of black carbon aerosol using particle-resolved model simulations with PartMC-MOSAIC. We developed number-based and mass-based aging time-scales using the activation of the particles at a given supersaturation as a criterion for aging. We applied this method to an urban plume scenario (Riemer et al., 2009) for a range of supersaturation thresholds between 0.01% and 10% and considered condensation of secondary substances and coagulation as aging mechanisms. Aging due to heterogeneous processes (chemical aging) were not included.

For this particular scenario we found a separation into day and night regimes. During the day the condensation-induced aging dominated, in particular due to the formation of ammonium nitrate. Therefore the condensation-only number-based aging time-scale $\tau_{N,day}^{cond}$ was almost the same as the total time-scale $\tau_{N,day}$ and similarly for mass. The daytime aging number-based time-scale $\tau_{N,day}$ was about 11 h for a supersaturation threshold of $S_c = 0.1\%$ and decreased to 0.47 h for a threshold of $S_c = 0.6\%$. The daytime mass-based aging time-scale $\tau_{M,day}$ was about a factor of 3–4 lower than $\tau_{N,day}$ for all supersaturation thresholds.

During the night, the absence of condensable species caused the number-based aging time-scale $\tau_{N,night}$ to be about one order of magnitude larger than during the day. Coagulation became dominant, which was reflected by the fact that the condensation-only time-scale $\tau_{N,night}^{cond}$ was at least one order of magnitude larger than the total time-scale $\tau_{N,night}$. The nighttime aging time-scales therefore depended on the particle number concentrations. We suspect that chemical aging would have its largest impact during periods when condensation is not dominant, i.e. during the night in our case.

Differences in the mass-based aging time-scale τ_M and the number-based aging time-scale τ_N reflect the size-dependence of aging due to condensation versus coagulation. During the day, when condensation is dominant, τ_M is smaller than τ_N, since larger particles age faster due to condensation and τ_M is weighted more towards the larger particles. During the night, when coagulation is dominant, τ_N is smaller than τ_M, since coagulation is faster for the smaller fresh particles and τ_N is weighted more towards the smaller particles.

Compared to the time-scales used in global models, which are typically on the order of 30 h (Chung & Seinfeld, 2002; Koch, 2001, e.g.), our time-scales were shorter, in particular during the day. This confirmed findings by Riemer et al. (2004) who showed with a completely different approach that daytime and nighttime aging regimes exists, and that aging during the day proceeds very rapidly.

However, some caveats need to be emphasized: Our urban plume scenario represents only one scenario, with very polluted conditions, including large amounts of ammonium nitrate during the day and fairly high number concentrations during the night ($N_{BC} \approx 5000\,cm^{-3}$). For lower number concentrations, we expect the aging time-scales during the night to increase. Our results indicate that the aging time-scales are strongly dependent on the supersaturation threshold, which in turn is influenced by several factors including cloud dynamics and the concentration of aerosol particles as the compete for available water vapor.

References

Andreae, M., & Gelencśer, A. (2006). Black carbon or brown carbon? The nature of light-absorbing carbonaceous aerosols. *Atmospheric Chemistry and Physics*, *6*, 3131–3148.

Bond, T., Streets, D., Yarber, K., Nelson, S., Woo, J., & Klimont, Z. (2004). A technology-based global inventory of black and organic carbon emissions from combustion. *Journal of Geophysical Research*, *109*(D14), D14203.

Brent, R. P. (2002). *Algorithms for minimization without derivatives*. Dover Publications.

Chung, S. H., & Seinfeld, J. H. (2002). Global distribution and climate forcing of carbonaceous aerosols. *Journal of Geophysical Research*, *107*.

Clegg, S., Brimblecombe, P., & Wexler, A. (1998). Thermodynamic model of the system $H^+-NH_4^+-Na^+-SO_4^{2-}-NH_3-Cl^--H_2O$ at 298.15 K. *Journal of Physical Chemistry A*, *102*(12), 2155–2171.

Cooke, W. F., Liousse, C., Cachier, H., & Feichter, J. (1999). Construction of a $1° \times 1°$ fossil fuel emission data set for carbonaceous aerosol and implementation and radiative impact in the ECHAM4 model. *Journal of Geophysical Research*, *104*, 22137–22162.

Croft, B., Lohmann, U., & von Salzen, K. (2005). Black carbon aging in the Canadian Centre for Climate modelling and analysis atmospheric general circulation model. *Atmospheric Chemistry and Physics*, *5*, 1931–1949 (sRef-ID:1680-7324/acp/2005-5-1931).

Cubison, M. J., Ervens, B., Feingold, G., Docherty, K. S., Ulbrich, I. M., Shields, L. et al. (2008). The influence of chemical composition and mixing state on Los Angeles urban aerosol on CCN number and cloud properties. *Atmospheric Chemistry and Physics. Discussions*, *8*, 5629–5681.

El Samad, H., Khammash, M., Petzold, L., & Gillespie, D. (2005). Stochastic modeling of gene regulatory networks. *International Journal of Robust and Nonlinear Control*, *15*(15), 691–711.

Eldering, A., & Cass, G. R. (1996). Source-oriented model for air pollution effects on visibility. *Journal of Geophysical Research*, *101*, 19343–19369.

Furutani, H., Dallosto, M., Roberts, G., & Prather, K. (2008). Assessment of the relative importance of atmospheric aging on CCN activity derived from field observations. *Atmospheric Environment*, *42*(13), 3130–3142.

Ghan, S., Laulainen, N., Easter, R., Wagener, R., Nemesure, S., Chapman, E., Zhang, Y., & Leung, R. (2001). Evaluation of aerosol direct radiative forcing in MIRAGE. *Journal of Geophysical Research*, *106*(D6), 5317–5334.

Gillespie, D. T. (1975). An exact method for numerically simulating the stochastic coalescence process in a cloud. *Journal of the Atmospheric Sciences*, *32*, 1977–1989.

Gillespie, D. T. (1976). A general method for numerically simulating the stochastic time evolution of coupled chemical reactions. *Journal of Computational Physics*, *22*, 403–434.

Gillespie, D. T. (1977). Exact stochastic simulation of coupled chemical reactions. *Journal of Physical Chemistry*, *81*, 2340–2361.

Gillespie, D. T. (1992). *Markov processes: An introduction for physical scientists*. New York: Academic Press.

Gillespie, D. T. (2007). Stochastic simulation of chemical kinetics. *Annual Review of Physical Chemistry*, *58*, 35–55.

Horvath, H., & Trier, A. (1993). A study of the aerosol of Santiago de Chile—I. Light extinction coefficient. *Atmospheric Environment*, *27*, 371–384.

IPCC (2007). *Climate change 2007: The physical science basis summary for policymakes*. Contribution of working group I to the fourth assessment report of the Intergovernmental Panel on Climate Change. World Meteorological Organization, Geneva, Switzerland.

Jaenicke, R. (1993). Tropospheric aerosols. *Aerosol-cloud-climate interaction* (pp. 1–31). San Diego, CA: Academic Press.

Kittelson, D., Watts, W., & Johnson, J. (2006). On-road and laboratory evaluation of combustion aerosols—part 1: Summary of diesel engine results. *Aerosol Science*, *37*, 913–930.

Kittelson, D., Watts, W., Johnson, J., Schauer, J., & Lawson, D. (2006). On-road and laboratory evaluation of combustion aerosols—part 2: Summary of spark ignition engine results. *Aerosol Science*, *37*, 931–949.

Kleeman, M., Schauer, J., & Cass, G. (2000). Size and composition distribution of fine particulate matter emitted from motor vehicles. *Environmental Science and Technology*, *34*, 1132–1142.

Koch, D. (2001). Transport and direct radiative forcing of carbonaceous and sulfate aerosols in the GISS GCM. *Journal of Geophysical Research*, *106*, 20311–20332.

Lohmann, U., Feichter, J., Chuang, C. C., & Penner, J. E. (1999). Prediction of the number of cloud droplets in the ECHAM GCM. *Journal of Geophysical Research*, *104*, 9169–9198.

McFiggans, G., Artaxo, P., Baltensperger, U., Coe, H., Facchini, M. C., Feingold, G. et al. (2006). The effect of physical and chemical aerosol properties on warm cloud droplet activation. *Atmospheric Chemistry and Physics*, *6*, 2593–2649.

McMurry, P., & Stolzenburg, M. (1989). On the sensitivity of particle size to relative humidity for Los Angeles aerosols. *Atmospheric Environment (1967)*, *23*(2), 497–507.

Medalia, A., & Rivin, D. (1982). Particulate carbon and other components of soot and carbon black. *Carbon*, *20*, 481–492.

Menon, S., Hansen, J., Nazarenko, L., & Luo, Y. F. (2002). Climate effects of black carbon aerosols in China and India. *Science*, *297*, 2250–2253.

Moffet, R., Qin, X., Rebotier, T., Furutani, H., & Prather, K. (2008). Chemically segregated optical and microphysical properties of ambient aerosols measured in a single-particle mass spectrometer. *Journal of Geophysical Research*, *113*(D12), D12213.

Nam, E., Fulper, C., Warila, J., Somers, J., Michaels, H., Baldauf, R., et al. (2008). *Analysis of particulate matter emissions from light-duty gasoline vehicles in Kansas City*. Technical report EPA420-R-08-010, United States Environmental Protection Agency.

Petters, M., Prenni, A., Kreidenweis, S., DeMott, P., Matsunaga, A., Lim, Y. et al. (2006). Chemical aging and the hydrophobic-to-hydrophilic conversion of carbonaceous aerosol. *Geophysical Research Letters*, *33*, L24806.

Petters, M. D., & Kreidenweis, S. M. (2007). A single parameter representation of hygroscopic growth and cloud condensation nucleus activity. *Atmospheric Chemistry and Physics*, *7*, 1961–1971.

Pöschl, U. (2005). Atmospheric aerosols: Composition, transformation, climate and health effects. *Angewandte Chemie International Edition in English*, *44*, 752–754.

Prenni, A., Petters, M., Kreidenweis, S., DeMott, P., & Ziemann, P. (2007). Cloud droplet activation of secondary organic aerosol. *Journal of Geophysical Research*, *112*, D10223.

Press, W. H., Teukolsky, S. A., Vetterling, W. T., & Flannery, B. P. (2007). *Numerical recipes: The art of scientific computing*. 3rd ed., Cambridge: Cambridge University Press.

Riemer, N., Vogel, H., & Vogel, B. (2004). Soot aging time scales in polluted regions during day and night. *Atmospheric Chemistry and Physics*, *4*, 1885–1893.

Riemer, N., Vogel, H., Vogel, B., & Fiedler, F. (2003). Modeling aerosols on the mesoscale γ, part I: Treatment of soot aerosol and its radiative effects. *Journal of Geophysical Research*, *108*, 4601.

Riemer, N., West, M., Zaveri, R., & Easter, R. (2009). Simulating the evolution of soot mixing state with a particle-resolved aerosol model. *Journal of Geophysical Research*, *114*, D09202.

Robert, M. A., Kleeman, M. J., & Jakober, C. A. (2007). Size and composition distributions of particulate matter emissions: Part 2—heavy-duty diesel vehicles. *Journal of Air & Waste Management Association*, *57*, 1429–1438.

Rudich, Y., Donahue, N. M., & Mentel, T. F. (2007). Aging of organic aerosol: Bridging the gap between laboratory and field studies. *Annual Review of Physical Chemistry*, *58*, 321–352.

Schell, B., Ackermann, I. J., Binkowski, F. S., & Ebel, A. (2001). Modeling the formation of secondary organic aerosol within a comprehensive air quality model system. *Journal of Geophysical Research*, *106*, 28275–28293.

Somers, J. (2004). Mobile source black carbon emissions. In: *Black carbon emissions and climate change: A technical workshop*. United States Environmental Protection Agency.

Svenningsson, B., Rissler, J., Swietlicki, E., Mircea, M., Bilde, M., Facchini, M. et al. (2006). Hygroscopic growth and critical supersaturations for mixed aerosol particles of inorganic and organic compounds of atmospheric relevance. *Atmospheric Chemistry and Physics*, *6*, 1937–1952.

Toner, S., Sodeman, S., & Prather, K. (2006). Single particle characterization of ultrafine and accumulation mode particles from heavy duty diesel vehicles using aerosol time-of-flight mass spectrometry. *Environmental Science and Technology*, *40*, 3912–3921.

Weingartner, E., Burtscher, H., & Baltensperger, H. (1997). Hygroscopic properties of carbon and diesel soot particles. *Atmospheric Environment*, *31*, 2311–2327.

Wells, C., Morgan, N., Kraft, M., & Wagner, W. (2006). A new method for calculating the diameters of partially-sintered nanoparticles and its effect on simulated particle properties. *Chemical Engineering Science*, *61*, 158–166.

Zaveri, R. A., Easter, R. C., Fast, J. D., & Peters, L. K. (2008). Model for simulating aerosol interactions and chemistry (MOSAIC). *Journal of Geophysical Research*, *113*, D13204.

Zaveri, R. A., Easter, R. C., & Peters, L. K. (2005). A computationally efficient multicomponent equilibrium solver for aerosols (MESA). *Journal of Geophysical Research*, *110*, D24203.

Zaveri, R. A., Easter, R. C., & Wexler, A. S. (2005). A new method for multicomponent activity coefficients of electrolytes in aqueous atmospheric aerosols. *Journal of Geophysical Research*, *110*, D02210.

Zaveri, R. A., & Peters, L. K. (1999). A new lumped structure photochemical mechanism for large-scale applications. *Journal of Geophysical Research*, *104*, 30387–30415.